Article

Not peer-reviewed version

Multi-Ion Modeling and Experiments Enable Consistent, High-Throughput Microcavity Array Generation via Mask Electrolyte Jet Machining

Ming Wu , Zhongning Guo , Jun Qian , Dominiek Reynaerts *

Posted Date: 8 October 2022

doi: 10.20944/preprints202210.0089.v1

Keywords: micro surface structures; mask electrolyte jet machining; electrochemical micro machining

Article

Multi-Ion Modeling and Experiments Enable Consistent, High-Throughput Microcavity Array Generation via Mask Electrolyte Jet Machining

Ming Wu [1,2], Zhongning Guo [3], Jun Qian[1,2], and Dominiek Reynaerts [1,2]*

[1] Department of Mechanical Engineering, KU Leuven, Oude Markt 13, Leuven 3000, Belgium
[2] Flanders Make, Belgium, Leuven 3000, Belgium
[3] College of Mechanical and Electircal Engineering, Guangdong University of Technology, Guangzhou 510006, China
* Correspondence: dominiek.reynaerts@kuleuven.be

Abstract: The controllability and consistency in the fabrication of micro-textures on large-scale remains a challenge for existing production processes. Mask electrolyte jet machining (MEJM) is an alternative to Jet-ECM for controllable and high-throughput surface microfabrication with more consistency of dimensional tolerances. This hybrid configuration combines the high-throughput of masked-ECM and the adjustable flow-field of jet-ECM. In this work, a duckbill jet nozzle was introduced to make MEJM more capable of batch micro-structuring. A multiphysics model was built to simulate the distribution of electrochemical reaction ions, the current density distribution, and the evolution of the shape of the machined cavity. Experimental investigations are presented showing the influence of the machining voltage and nozzle moving speed on the micro cavity. Several 35×35 micro cavity arrays with a diameter of $24.92 - 11.73$ µm and depth of $15.86 - 7.24$ µm are generated on 304 stainless steel.

Keywords: micro surface structures; mask electrolyte jet machining; electrochemical micro machining

1. Introduction

Micro cavity arrays, as a typical surface microstructure, are broadly applicable such as for heat exchangers[1,2], friction and wear[3], anti-fouling[4,5] , etc. Recently, it has been reported that cutting tools[6,7] textured with micro cavities could reduce the cutting force, average friction coefficient, and cutting tool wear, which is useful for machining difficult-to-machine materials. Currently, several technologies have been introduced to manufacture micro cavities on metallic surfaces, such as femtosecond laser micromachining[8], micro-milling[9] and micro-electrical discharge machining[10].

Compared to the aforementioned methods, electrochemical micromachining (EMM) [11] is a promising method for preparing micro cavities[12], as it has unique advantage such as a good control on cavity profile, the potential for multi-response optimization[13], independence of material hardness[14] and toughness[15], absence of a heat-affected layer, lack of process related tool wear and burrs, and a high throughput capability. Through-mask electrochemical micromachining (TMEMM) is a promising method for generating array-like surface microstructures. In this method, the workpiece surface is covered by a patterned mask, and the machining region is exposed. Subsequent electrochemical micromachining dissolves the exposed area to create the surface texture. With this method, several kinds of surface texture can be prepared, such as micro cavity arrays and micro groove arrays[16]. Wang et al. [17] reported fabrication of a micro cavity array with a diameter of 40 µm diameter on a metallic cylindrical surface by using TMEMM. In the work of Qu et al.[18], a dry-film photoresist was used as a mask during through-mask electrochemical micromachining to successfully fabricate micro cavity arrays (each cavity about 94 µm in diameter and 22.7 µm deep) on inner cylindrical surfaces. Qu[19] proposed a modified micro-scale pattern transfer without involving photolithography of substrates. In their work, a through movable dry-film mask electrochemical micromachining was employed for fabrication of micro cavities of 109.4 µm in diameter and 15.1 µm in depth.

Besides the aforementioned masked-ECM methods, Jet electrochemical machining (Jet-ECM) has also been shown to be an effective approach for generating deep micro cavities[20]. The unique characteristic of this technology is that the electrolyte is ejected from the metallic nozzle to the workpiece with high velocity, which is helpful for preparing deep micro cavities as the electrolyte in the micro cavity can be renewed rapidly[21]. Jet-ECM has been used to fabricate micro-grooves and micro cavities, showing it to be a flexible method[22]. Hackert et al.[23] employed Jet-ECM for generating micro cavities by using a metallic nozzle with an inner diameter of 100 μm. As the depth increased from 37 μm to 90 μm, the diameter of the micro cavity was enlarged from 173 μm to 220 μm, and the machining localization was reduced. Because the workpiece surface is exposed to jet without side insulation, it often leads to undercutting and stray corrosion at the edge of the micro cavity, and the phenomenon is worsening with an increase in depth, which reduces the machining accuracy and surface quality. Yan [24] presented a reciprocating electrolyte jet machining technology with prefabricated mask (REJP) which was used to generate a circular cavity array of about 43 μm in depth and 822 μm in diameter on a cast-iron cylinder liner.

These aforementioned methods exhibit a rather low machining efficiency and do not meet the requirements of mass-fabrication of micro cavity like micro-structures. For efficient electrochemical machining of micro cavity array structures, enhanced electrolyte renewal can be helpful for machining high aspect ratio cavities, and reducing the undercutting can improve the machining localization. Mask electrolyte jet machining (MEJM) is an alternative to Jet-ECM/TMEMM for surface microfabrication with more consistency of dimensional variation[25,26]. MEJM is a hybrid configuration which combines the advantages of through-mask electrochemical machining, which is a high-throughput process, and of jet electrochemical machining, with its adjustable flow field.

In the present work, a duckbill jet nozzle is introduced to make MEJM more capable of batch micro-structuring. A multiphysics model is developed to simulate the electric field distribution and micro cavity forming process of the electrolyte. Experimental investigations regarding the influences of machining voltage and nozzle moving speed on the micro cavity are presented. Optimization of the experimental parameters is performed. Finally, the efficient machining of a high number of micro cavities on a stainless-steel plate is demonstrated.

2. Process Principle and Theoretical Analysis

2.1. Process principle

The schematic view of MEJM using a duckbill nozzle is shown in Fig. 1 (a). During the machining process, the high-speed electrolyte is sprayed from the metallic nozzle and the nozzle scans on the workpiece. Meanwhile, the high- speed electrolyte flow reaches the exposed workpiece through the micro holes in the mask. Finally, a micro cavity array can be generated when a sufficient voltage is applied between the metallic nozzle and the workpiece. More specifically, a metallic nozzle was employed to provide a stable and high-speed jet flow for workpiece and the renewal of electrolyte in the small machining area, which was useful for generating deep micro cavities. This method is highly flexible and enables machining of large areas.

A finite element model (FEM) is developed to investigate the electric field and current density distribution on the workpiece. The profile evolution of the micro cavities can be predicted by this FEM. A 2D diagram of this process configuration is shown in Fig. 1 (b), the geometric and simulation parameters of the model are listed in Table 1.

During machining, the electrolytic products and joule heat will be rapidly removed from the machining area by a high velocity flow of electrolyte. Therefore, the heat effects in the electrochemical reactions do not need to be considered in this case. One of the most significant features of MEJM is the electrolyte flow direction that is changing over time, which refers to a changing concentration gradient in the bulk electrolyte. The current density $\vec{J}$ in the electrochemical cell can be represented by the ion transportation:

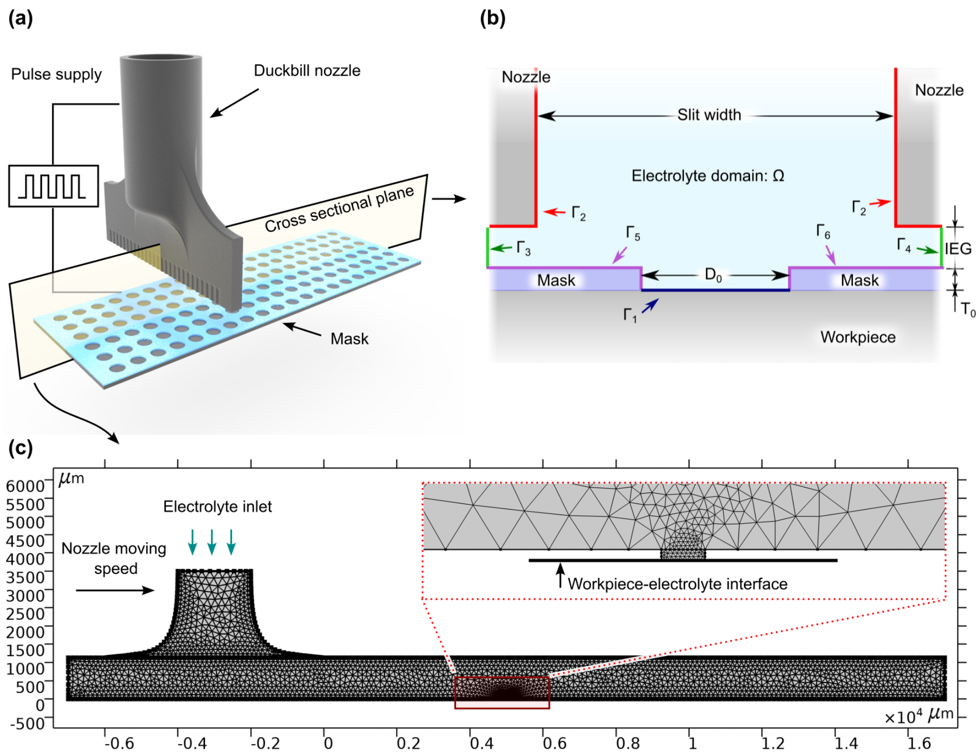

Figure 1. (a) MEJM process schematic view; (b) The 2D model diagram of MEJM; (c) FEM simulation geometry and mesh

Model parameters	Value
Diameter of the dimple in the mask, D_0	5 μm
Thickness of the mask, T_0	1.2 μm
Inter-electrode gap, IEG	3.5 mm
Duckbill nozzle slit length,	16 mm
Duckbill nozzle slit width,	0.5 mm
Density of electrolyte, ρ	$1100\,\mathrm{kg/m^3}$
Electrolyte temperature, T	298 K
Electrolyte conductivity, σ	10 S/m
Faraday constant, F	96486 C/mol
Applied voltage, U	10 V
Nozzle moving speed, v	2 mm/s
Molar gas constant, R	$8.314472\,\mathrm{J/(K \cdot mol)}$

Table 1. The parameter of simulation

Species i	Diffusion coefficient D_i ($10^{-9}\,\mathrm{m}^2/\mathrm{s}$)
Na^+	1.33
$NO_3{}^-$	1.90
H^+	9.31
OH^-	5.26
Fe^{3+}	1.24

Table 2. Diffusion coefficients at 293.15 K

$$\vec{J} = F \sum z_i \vec{N_i} \tag{1}$$

where z_i is the valence for species i, and $\vec{N_i}$ is the flux of ions which is the result from:

1 Diffusion: $\vec{N_D}$

$$N_D = -D_i \nabla c_i \tag{2}$$

where D_i is the diffusion coefficient, c_i the concentration. Here, H^+, OH^-, Na^+, NO_3 and Fe^{3+} were the ions taking part in the electrochemical reactions, the diffusion coefficients are shown in Table 2

2 Convection: $\vec{N_C}$

$$N_C = \vec{u} c_i \tag{3}$$

where $\vec{u}$ is the velocity field. In this case, the electrolyte flow rate is considered as laminar flow and can hence be represented by the Navier-Stokes equation:

$$\begin{cases} \rho \dfrac{\partial \vec{u}}{\partial t} + \rho(\vec{u} \cdot \nabla)\vec{u} = -\nabla p + \mu \Delta \vec{u} + \rho \vec{g} \\ \dfrac{\partial \rho}{\partial t} + \rho \nabla \vec{u} = 0 \end{cases} \tag{4}$$

3 Electric migration: $\vec{N_E}$

$$N_E = -\frac{F D_i z_i ci}{RT} \nabla \phi \tag{5}$$

where F is the Faraday constant, R the ideal gas constant, T the temperature and ϕ the electric potential in the interelectrode gap, which can be described by Laplace's equation with a number of certain boundary conditions:

$$\begin{cases} \nabla^2 \phi & = \dfrac{\partial^2 u}{\partial x^2} + \dfrac{\partial^2 u}{\partial y^2} = 0 \\ \phi \mid_{\Gamma_0} & = 0V(\text{Anode boundaries}) \\ \phi \mid_{\Gamma_3} & = 10V(\text{Cathode boundaries}) \\ \dfrac{\partial \phi}{\partial \vec{n}} \mid_{\Gamma_0} & = 0V(\text{Insulation boundaries}) \end{cases} \tag{6}$$

where $\vec{n}$ is the normal phase vector of the boundary.

Therefore, the flux $\vec{N_i}$ of species in the electrolyte can be given by (7):

$$\begin{aligned} \vec{N_i} &= \vec{N_D} + \vec{N_C} + \vec{N_E} \\ &= -D_i \nabla c_i + \vec{u} c_i - \frac{F D_i z_i ci}{RT} \nabla \phi \end{aligned} \tag{7}$$

The boundary conditions for the ion transportation are as follows:

- Inflow(inlet):

$$\begin{cases} \vec{u} = \vec{u_0} \\ c_i = c_{i,0} \end{cases} \tag{8}$$

- Outflow(outlet):

$$\begin{cases} p = 0 \\ \vec{n} \cdot D_i \nabla c_i = 0 \end{cases} \tag{9}$$

- Open boundary:
  - As no viscous stress is set for the laminar flow, it does not impose any constraint on the pressure:

$$\mu(\nabla\vec{u} + (\nabla\vec{u})^T) \cdot \vec{n} = 0 \tag{10}$$

  - For the ion transportation:

$$\begin{cases} -\vec{n} \cdot \vec{N_i} = 0, & \vec{n} \cdot \vec{u} \geqslant 0 \\ c_i = c_{i,0}, & \vec{n} \cdot \vec{u} < 0 \end{cases} \tag{11}$$

- Anode:

$$\mathrm{Fe} + 2\,\mathrm{H_2O} \longrightarrow \mathrm{Fe}^{3+} + \mathrm{O}^{2} + 4\,\mathrm{H}^{+} + 7\,\mathrm{e}^{-} \tag{12}$$

- Cathode:

$$2\,\mathrm{H_2O} + 2\,\mathrm{e}^{-} \longrightarrow \mathrm{H_2} + 2\,\mathrm{OH}^{-} \tag{13}$$

According to Faraday's law, the normal dissolution velocity $\vec{v_n}$ on the anode boundary can be given by:

$$\vec{v_n} = \eta \frac{M}{zF} \vec{J} \tag{14}$$

where M is the molar mass of the workpiece material.

By solving (2), (3), (5), (6) and (14), the electric field, current density distribution and the material removal process can be calculated.

The numerical simulation model is built as shown in Fig. 1 (b) and Fig. 1 (c). As the mask shows no deformation during machining, a virtual gap with 0.1 µm is set between mask and workpiece to ensure the anode boundary to move properly. The model was built using a free triangular mesh, and the deformed region was refined to improve the calculation accuracy. In this work, the numerical simulations were performed by COMSOL.

2.2. Simulation results

The profile evolution and corresponding current density norm distribution on the reaction interface can be seen in Fig. 2, the diameter and depth of the machined cavity increased as the electrochemical reaction progressed. Because of the "edge effect" in the electric field, at t = 0s, the current density norm was slightly higher in the boundary between the photoresist and workpiece than that in the center of micro cavity.

Later in the process, the distribution is inverted, the current density is then always higher in the center than that in the boundary. This will lead to a concave-like profile, i.e. a micro cavity.

As the electrochemical dissolution reaction progressed, the depth of micro cavity was increasing, which is due to a larger distance between the anodic area on workpiece and cathode. In the meantime, the distance between the reaction interface and the nozzle, i.e. the cathode, is first reduced and then becomes longer again, the shortest distance between them was at the nozzle moving right above the reaction interface. In the presented simulation, the nozzle was right above the reaction interface at t = 2 s, as shown in Fig. A3, and the current density norm reached its peak value and then was reduced.

As shown in Fig. 3, the moving nozzle also changes the electrolyte flow direction both around and inside the machined cavity. The variation of the flow field and electric field will cause a variation of

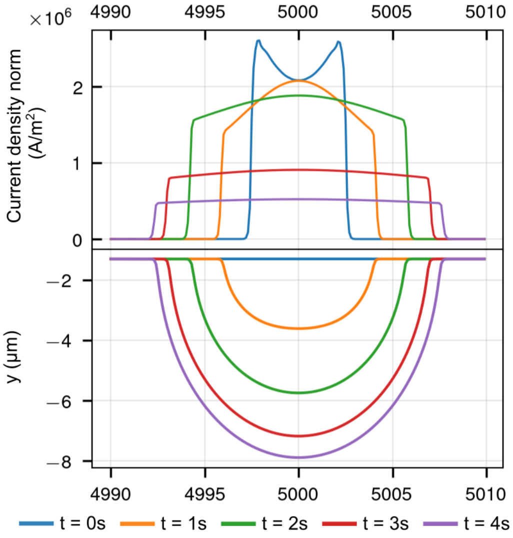

Figure 2. The profile evolution and corresponding current density norm on the reaction interface

the ion distribution. According to (5), positive ions will be repelled and negative ions will be attracted to the reaction interface since it is located at the surface of anode. Significantly more OH^- than H^+ around the reaction area, which refers to electrochemical reactions occur under an extreme alkaline environment. Similarly, more $NO_3{}^-$ than Na^+ ions were present in the reaction area. The produced Fe^{3+} ions were also expelled from the reaction interface. In the meantime, the neutral byproducts, such as $Fe(NO_3)_3$ cannot be removed from the reaction area by the electric migration effect. These neural byproducts can be driven out by convection and diffusion. The detailed simulation results at different machining times (t =0 s: Fig. A1; t =1 s: Fig. A2; t =2 s: Fig. A3; t =3 s:Fig. A4) are provided in Appendix A. Here, the varying flow field makes the byproducts less prone to accumulate, which is what MEJM envisages.

In Fig. 4, the profiles of cavity from simulation and experiment (for details, please see Section 3.1) are presented. The shape and depth of the features from the simulation demonstrated a good agreement with that from the experiments. However, the simulated and experimental micro cavity diameters are 6 µm and 8.13 µm, respectively. This indicates that while the depth of the micro cavity for experiments is higher, the undercutting is smaller than the simulation result. This may be because of the absence of pulsed current in our simulation, which can increase the localization of electrochemical reactions. Further work will focus on modelling of pulsed current and its effects on the electrical double layer.

3. Experimental Studies

3.1. Materials and metrics

The workpiece material for experimental investigations was 304 stainless steel, and it was polished to mirror surface(surface roughness <0.8 µm) to have uniform contact with the mask. The lithographic mask array holes are 5 µm in diameter. These micro-holes are distributed as a 35 × 35 square array, and the hole center-distance is 50 µm. The jet nozzle is implemented as a duckbill shaped nozzle with a slit length of 16 mm and a slit width of 0.5 mm.

The surface topography of the micro cavity structure was obtained with a scanning electron microscope (S-3400N(II)). The size of micro cavity was measured by a laser scanning confocal microscope (Olympus OLS-4100). From the upper left corner to the lower right corner of the workpiece, 35 positions along the diagonal were uniformly selected for measurements. The diameter (D_i) and depth (H_i) of micro cavities were measured. The aspect ratio (AR), the standard deviation of width and depth (S_w and S_H), and the etch factor (EF) were calculated, as shown in formulas (15) and (16).

$$AR = \frac{H_i}{D_i} \tag{15}$$

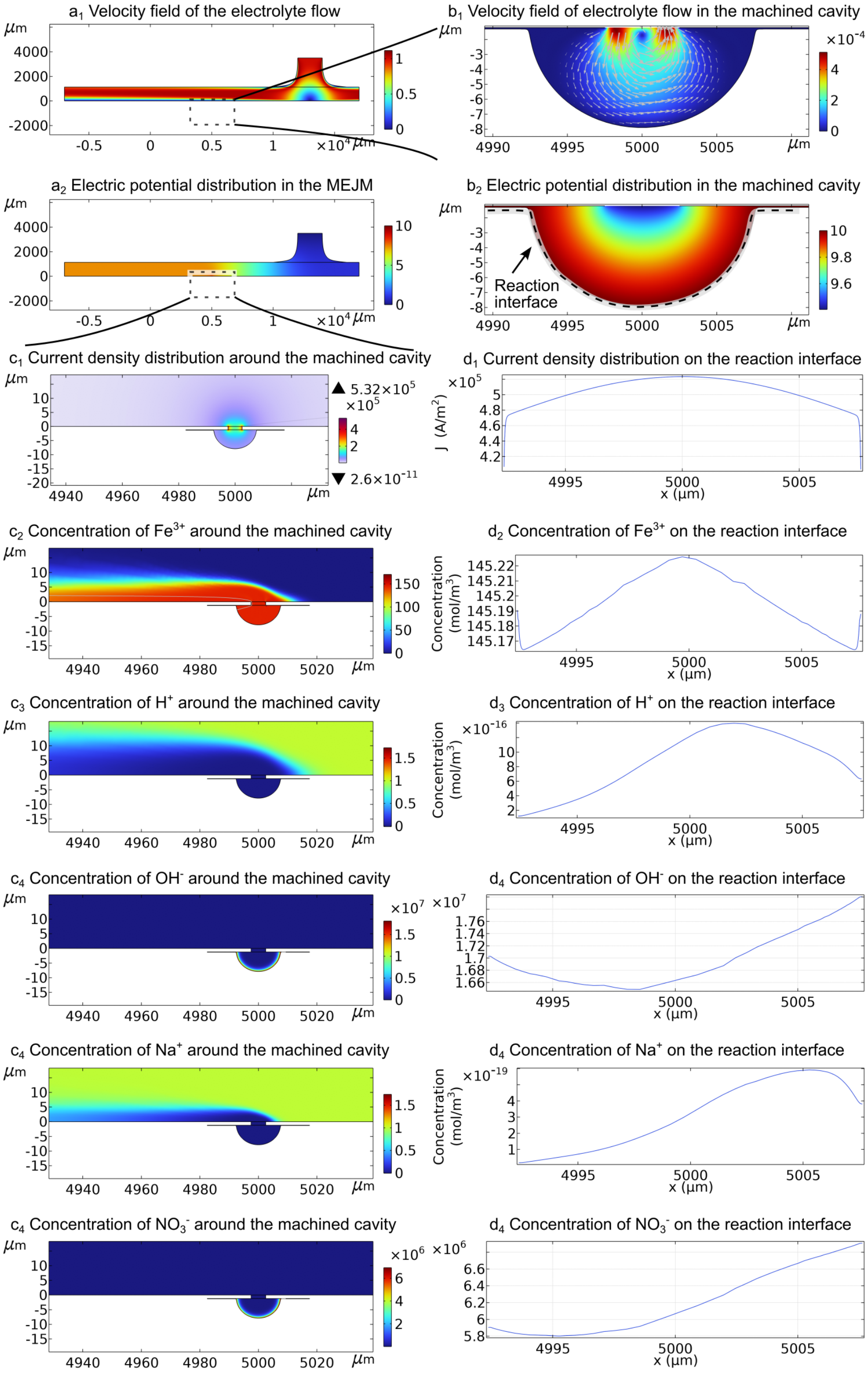

Figure 3. Simulation results @ t=4 s. (a_1): velocity field of the electrolyte flow; (b_1): velocity field of electrolyte flow in the machined cavity; (a_2) electric potential distribution in the MEJM; (b_2) electric potential distribution (A/m^2) in the machined cavity; (c_1) normal current density distribution around the machined cavity; (d_1): normal current density distribution on the reaction interface; (c_2) – (c_4): concentration (mol/m^3) of Fe^{3+}, H^+, OH^-, Na^+, and $NO_3{}^-$ around the machined cavity; (d_2) – (d_4): concentration (mol/m^3) of Fe^{3+}, H^+, OH^-, Na^+, and $NO_3{}^-$ on the reaction interface

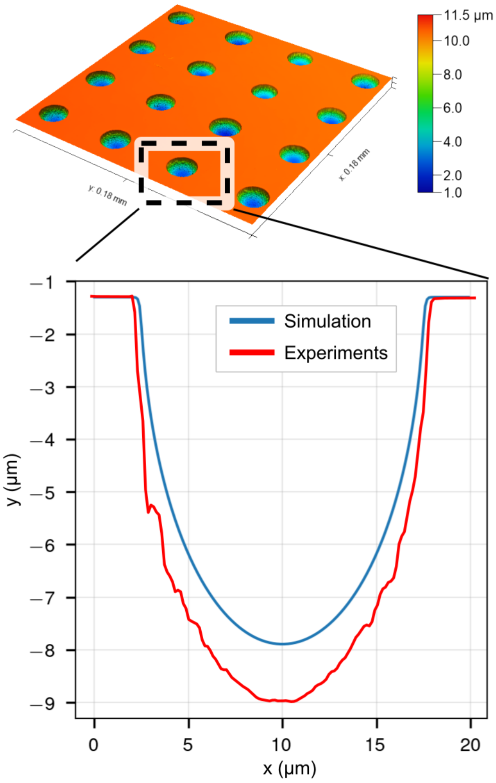

Figure 4. The cross sectional profile of cavities from simulation and experiments

Table 3. Experimental parameters

Parameters	Value
Applied voltage	10, 20, 30, 40 V
Pulse frequency	2 kHz
Pulse duty cycle	50%
Nozzle moving speed	1, 2, 3, 4 mm/s
Inter-electrode-gap	2mm
Electrolyte concentration	10 % (wt.%) aq. $NaNO_3$
Electrolyte temperature	25°C
Electrolyte pressure	20 kPa
Diameter of cavitys in the mask	5 µm
Mask thickness	1.2 µm
Workpiece material	Stainless steel 304

Preprints.org (www.preprints.org) | NOT PEER-REVIEWED | Posted: Posted: 8 October 2022 doi:10.20944/preprints202210.0089.v1

(a) Applied voltage=10 V, frequency=1 kHz, plus duty cycle=50%, nozzle moving speed=2 mm/s.

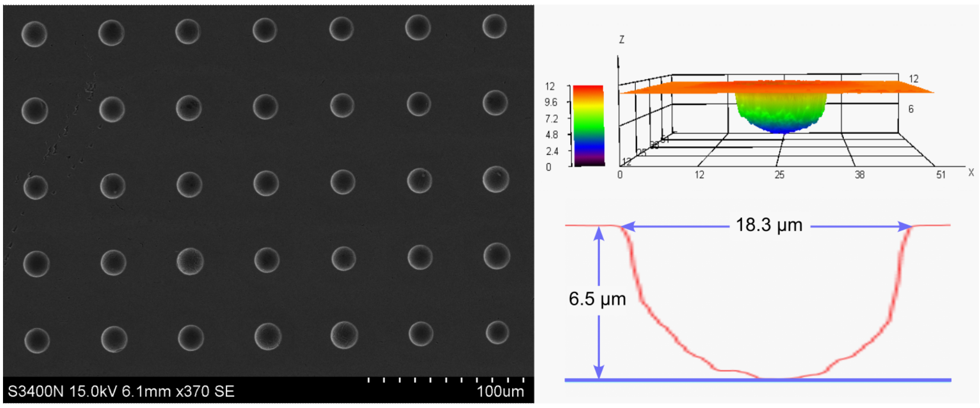

(b) Applied voltage=40 V, frequency=1 kHz, plus duty cycle=50%, nozzle moving speed=2 mm/s.

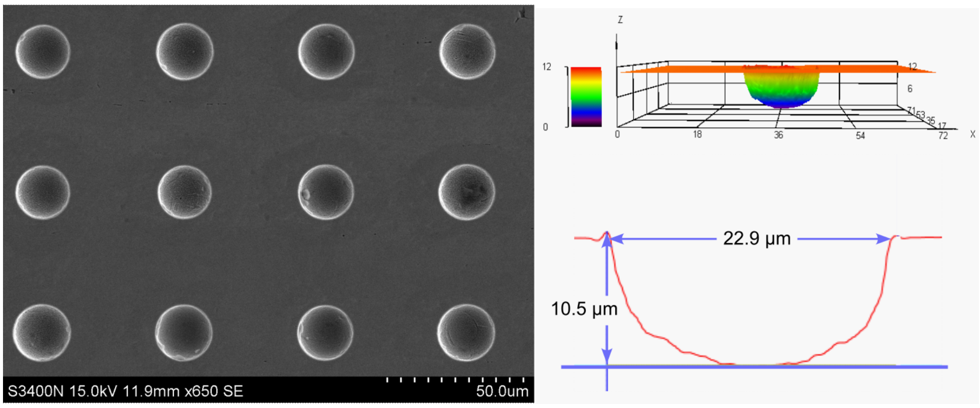

Figure 5. The typical profile of micro cavities at different applied voltage: (a) 10 V (b) 40 V

$$AR = \frac{2H_i}{D_i - D_0} \tag{16}$$

where D_0 is the diameter of cavities in the mask.

3.2. *Results and Discussion*

3.2.1. Influence of applied voltage

Voltages ranging from 10 V to 40 V were applied to investigate their effect on shape accuracy of micro cavity fabrication. A typical profile of a micro cavity array with good shape consistency and single micro cavity at different applied voltages (10 V and 40 V) are shown in Fig. 5.

Table 4. Diameter and depth of machined cavities with different applied voltage

Voltage (V)	10		20		30		40	
	D	H	D	H	D	H	D	H
mean	18.47	8.08	19.27	9.15	21.90	10.58	23.29	11.04
std	0.56	0.20	0.60	0.26	0.69	0.32	0.74	0.39
min	17.11	7.58	17.88	8.68	20.23	9.85	21.37	10.12
0.25	18.11	7.99	18.88	8.98	21.55	10.31	22.77	10.78
0.5	18.52	8.13	19.33	9.10	21.92	10.61	23.38	11.02
0.75	18.80	8.20	19.66	9.32	22.44	10.87	23.62	11.34
max	19.53	8.53	20.64	9.77	23.50	11.10	24.92	11.73

The dimensions of micro cavities generated with different applied voltage, with a pulse duty cycle of 50%, pulse frequency of 1 kHz, and a nozzle moving speed of 1 mm/s are shown in Fig. 6 and Table 4 . It can be seen that the diameter of micro cavities increased from 18.47 ± 0.56 µm (standard deviation)

doi:10.20944/preprints202210.0089.v1

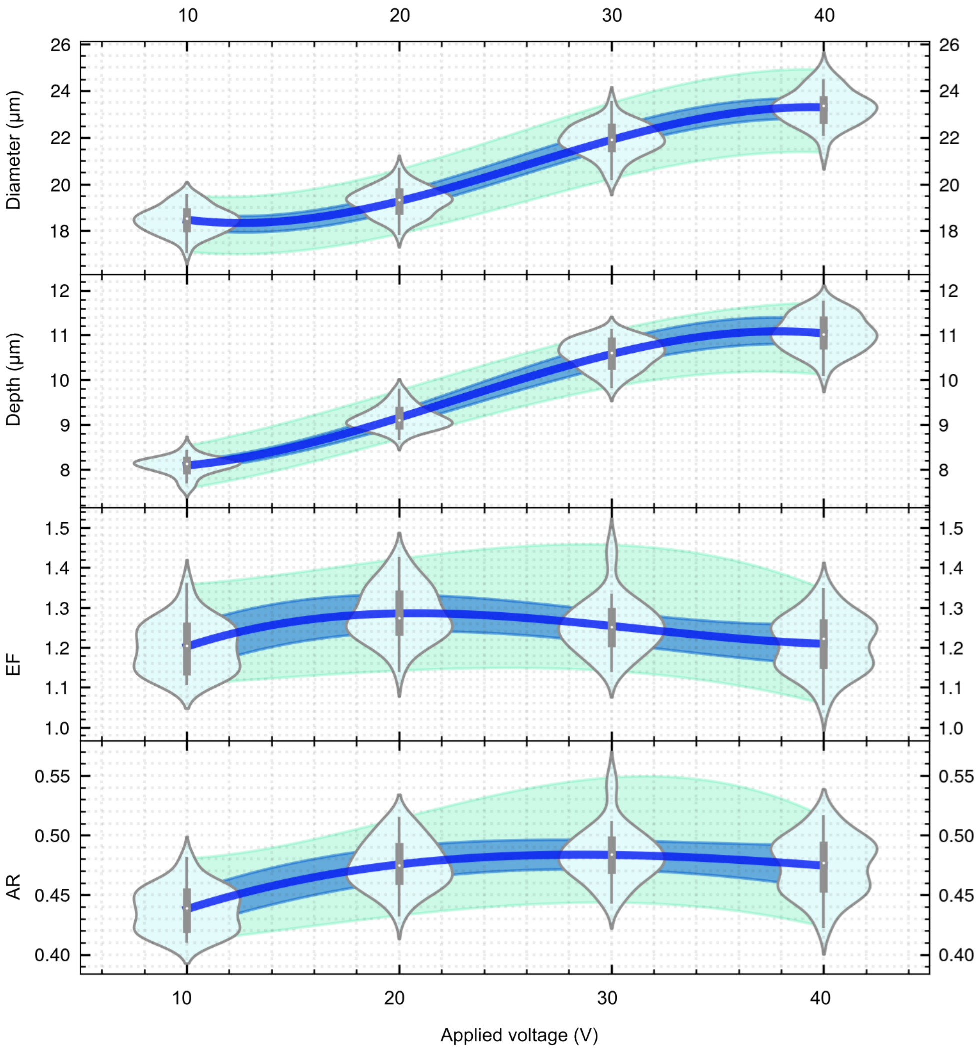

Figure 6. The effect of voltage on the dimensions of micro cavities

doi:10.20944/preprints202210.0089.v1

to 23.29 ± 0.74 µm as the voltage increased from 10 V to 40 V. Furthermore, the depth increased from 8.08 ± 0.02 µm to 11.04 ± 0.39 µm with an increase in voltage, thereby showing a similar trend as for the diameter. With an increase in voltage, the current density becomes higher. Therefore, the amount of material removal in a given machining time also increased. As a result, the diameter and depth of the micro cavities gradually increased, and the removal rate follows the general law of Faraday dissolution.

Table 5. EF and AR value of machined cavities with different applied voltage

Voltage (V)	10		20		30		40	
	EF	AR	EF	AR	EF	AR	EF	AR
mean	1.20	0.44	1.29	0.48	1.25	0.48	1.21	0.47
std	0.06	0.02	0.07	0.02	0.07	0.02	0.07	0.02
min	1.11	0.41	1.14	0.43	1.14	0.44	1.06	0.42
0.25	1.14	0.42	1.24	0.46	1.21	0.47	1.16	0.46
0.5	1.20	0.44	1.27	0.48	1.25	0.48	1.22	0.48
0.75	1.25	0.45	1.33	0.49	1.29	0.50	1.26	0.49
max	1.36	0.48	1.42	0.51	1.46	0.55	1.35	0.52

The values of the etch factor (EF) and the aspect ratio (AR) of the micro cavity at different voltages are shown in Fig. 6 and Table 5. As the voltage increased, the value of EF is around 1.202 and the aspect ratio of micro cavity ranges from 0.438 to 0.475. This shows that the presented MEJM process generates an aspect ratio that is higher than others described in the literature. The aspect ratio of micro cavities using through-mask electrochemical machining is about 0.1-0.2[27]. Hackert et al.[23] showed that by using Jet-ECM with a metallic nozzle of 100 µm inner diameter, the diameter of the micro cavity was 220 µm and the aspect ratio of micro cavity was 0.41.

It is worth mentioning that the standard deviations of diameter and depth slightly increased as the voltage increased. This indicates that the machining repeatability was reduced as the amount of removed material increased.

3.2.2. Influence of nozzle moving speed

A nozzle moving speed ranging from 1 m/s to 4 m/s was employed to investigate their effect on the shape accuracy of micro cavity fabrication. The typical profile of a micro cavity array with good shape consistency and single micro cavity at a different nozzle moving speed (2 mm/s and 4 mm/s) are shown in Fig. 7.

The diameter and depth of the micro cavities generated at different nozzle moving speed with an applied voltage of 30 V, a pulse duty cycle of 50%, and a pulse frequency of 2kHz are shown in Fig. 8. It can be seen that the diameter of the micro cavities decreased from 22.07 ± 0.71 µm to 17.21 ± 0.52 µm with an increase in nozzle moving speed from 1 mm/s to 4 mm/s. Furthermore, the depth decreases from 10.16 ± 0.31 µm to 7.70 ± 0.20 µm with an increase in nozzle moving speed. As the nozzle moving speed increases, it is equivalent to reducing the processing time, and thus the diameter and depth of the micro cavities has been reduced.

The value of EF and AR of the micro cavities using different nozzle moving speeds is shown in Fig. 8 and Table 7. Even at different nozzle moving speeds, the value of EF is around 1.2, showing the same trend as that for the voltage. The aspect ratio of the micro cavities ranges from 0.461 to 0.448. In this case, the EF of this MEJM technology is comparable to those observed in the literatures. Qu et al. [18] used a 50 µm thick dry-film photoresist as a mask during the TMEMM process to fabricate a micro cavity with an EF of 1.03 and 94 µm in diameter on a cylindrical inner surface, when the original mask aperture is 50 µm in diameter.

The standard deviations of diameter and depth were slightly decreased as the nozzle moving speed increased. This shows that the machining reliability was slightly increased as the amount

(a) Applied voltage=30 V, frequency=1 kHz, plus duty cycle=50%, nozzle moving speed=2 mm/s.

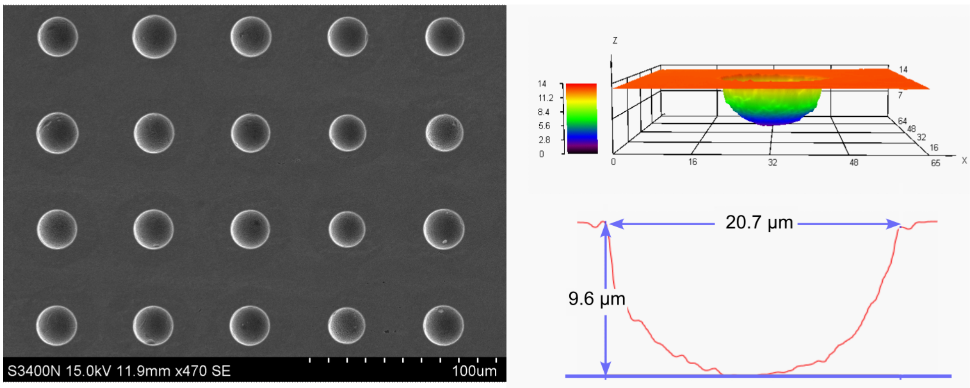

(b) Applied voltage=30 V, frequency=1 kHz, plus duty cycle=50%, nozzle moving speed=4 mm/s.

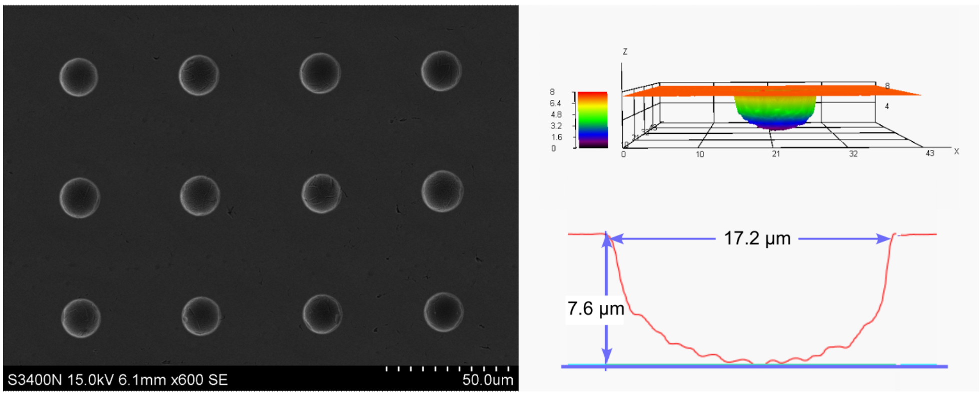

Figure 7. The typical profile of micro cavities at different nozzle moving speed: (a) 2 mm/s (b) 4 mm/s

Table 6. Diameter and depth of machined cavities with different nozzle moving speed

Speed (mm/s)	1		2		3		4	
	D	H	D	H	D	H	D	H
mean	22.07	10.16	20.91	10.16	19.55	9.10	17.21	7.70
std	0.71	0.31	0.66	0.26	0.60	0.23	0.52	0.20
min	20.37	9.40	19.38	9.68	18.08	8.58	15.86	7.24
0.25	21.63	10.02	20.48	9.99	19.24	8.92	16.84	7.57
0.5	22.13	10.24	20.98	10.10	19.56	9.13	17.27	7.69
0.75	22.48	10.33	21.35	10.33	20.02	9.31	17.44	7.85
max	23.40	10.83	22.43	10.78	20.96	9.48	18.36	8.04

Table 7. EF and AR of machined cavities with different nozzle moving speed

Speed (mm/s)	1.00		2.00		3.00		4.00	
	EF	AR	EF	AR	EF	AR	EF	AR
mean	1.19	0.46	1.28	0.49	1.25	0.47	1.26	0.45
std	0.07	0.02	0.06	0.02	0.06	0.02	0.07	0.02
min	1.10	0.43	1.14	0.44	1.15	0.43	1.12	0.41
0.25	1.13	0.44	1.23	0.47	1.21	0.45	1.21	0.43
0.5	1.20	0.46	1.27	0.48	1.25	0.47	1.28	0.45
0.75	1.25	0.48	1.33	0.50	1.29	0.48	1.31	0.46
max	1.35	0.51	1.41	0.52	1.45	0.52	1.42	0.48

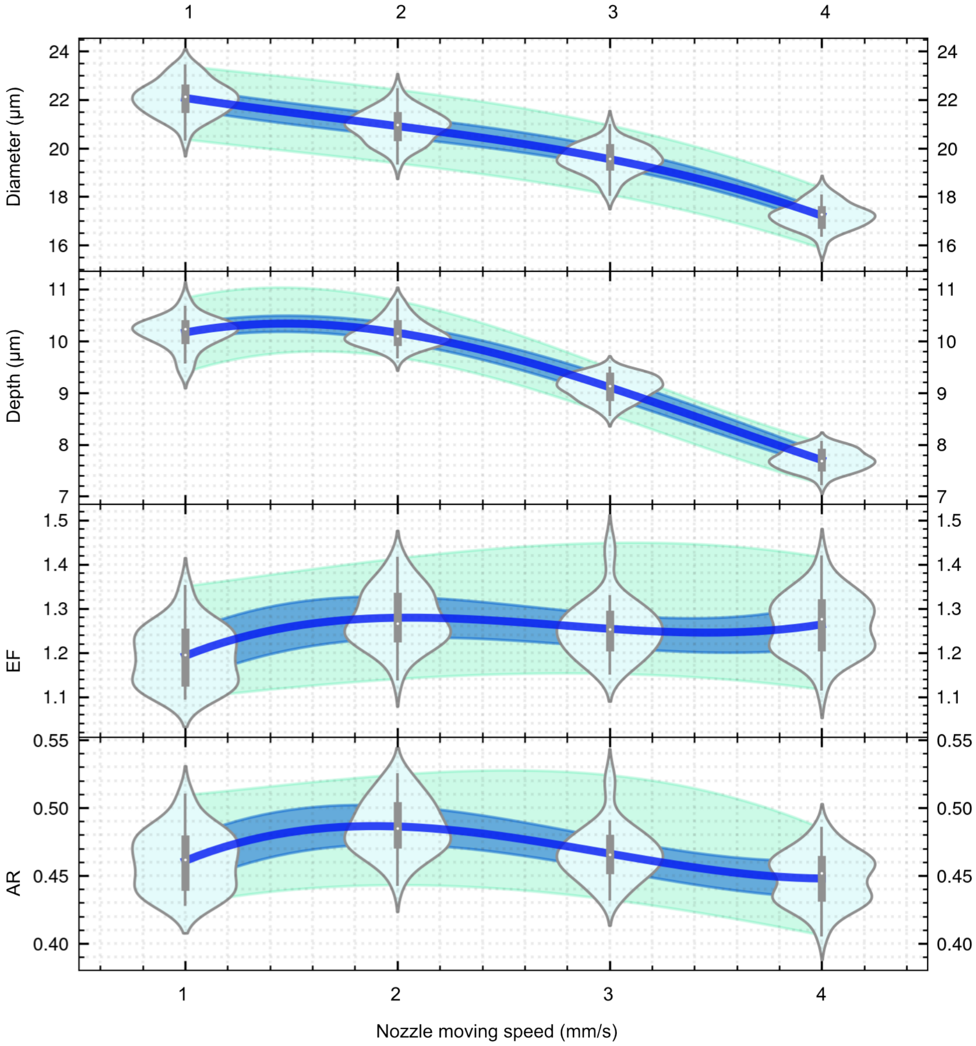

Figure 8. The effect of nozzle moving speed on the dimensions of micro cavities

of removed material increased. This is probably because of the deceased total machining time will decrease the risk of mask failure provoked by electrolyte flow flush.

4. Conclusion

In this study, a method of mask-based electrolyte jet machining with a duckbill nozzle was proposed for mass fabrication of a micron-sized micro cavity array on the surface of metal parts. The micro cavity shape evolution process and electric-field/current density distribution were simulated using COMSOL® Multiphysics software. A micro cavity array structure with a good shape and smooth contour was fabricated by MEJM. The design of experiments explored the influence of applied voltage and nozzle moving speed on the size and topography of the micro cavities. It can be concluded that the simulations showed good agreement with the experimental profile. However, there was less machining depth/more undercut in simulated profiles, possibly because of the absence of considering pulsed current.

It was observed in experiments that with an increase in process-voltage, the dimension of micro cavities and depth-to-diameter ratio gradually increased. The diameter and depth increased by 26.08% and 36.57% respectively, as the voltage increased from 10 V to 40 V. When the processing voltage is 40 V, the size of the micro cavities is highest. At low voltages, the micro cavities are shallow. Therefore, preference should be given to medium voltage. When the applied voltage is 20 V, the EF and AR values are the highest.

With an increase in the nozzle moving speed, the diameter and depth of the micro cavities are decreasing. The diameter and depth decreased by 22.04% and 24.23% respectively, as the nozzle moving speed increased from 1 mm/s to 4 mm/s. Meanwhile, the nozzle moving speed is not always leading to an increase in MEJM performance because of a reduced stability at high nozzle moving speed of the motion platform used in this study.

Overall, micro cavity structures were successfully fabricated using the proposed MEJM technology and a duckbill nozzle. This work is an initial step towards using MEJM technology for deterministic and efficient fabrication of micro-structures such as cavity/grooves on large workpieces. The technology can be further changed to texture curved and free-form surfaces using flexible masks. The technology has potential applications in the texturing of bearings for improved lubrication, mimicking of artificial bearing defects, micro-structuring of mould surfaces for improved ceramic/polymer injection molding. It is a tool-less process, so limitations on tool dimensions are overcome with this technology. The holes in the masks can be fabricated down to a nanometer scale using state-of-the-art lithography techniques. With improved electrolyte recycling systems, this technology can be a cost effective technology as it does not involve capital costs like for a laser texturing process using femto-second lasers, expensive optics and beam manipulation peripherals.

Author Contributions: Conceptualization, M.W.; methodology, M.W.; validation, M.W.; formal analysis, M.W.; investigation, M.W.; resources, Z.G.; writing—original draft preparation, M.W.; writing—review and editing, D.R.; visualization, M.W.; supervision, D.R. and Z.G.; project administration, D.R, Z.G. and J.Q.; funding acquisition, D.R. All authors have read and agreed to the published version of the manuscript.

Acknowledgments: This work was supported by the FLANDERS MAKE ICON Project 'ADAVI'.

Conflicts of Interest: The authors declare no conflict of interest.

Appendix A. Simulation results of ion distribution at different processing time

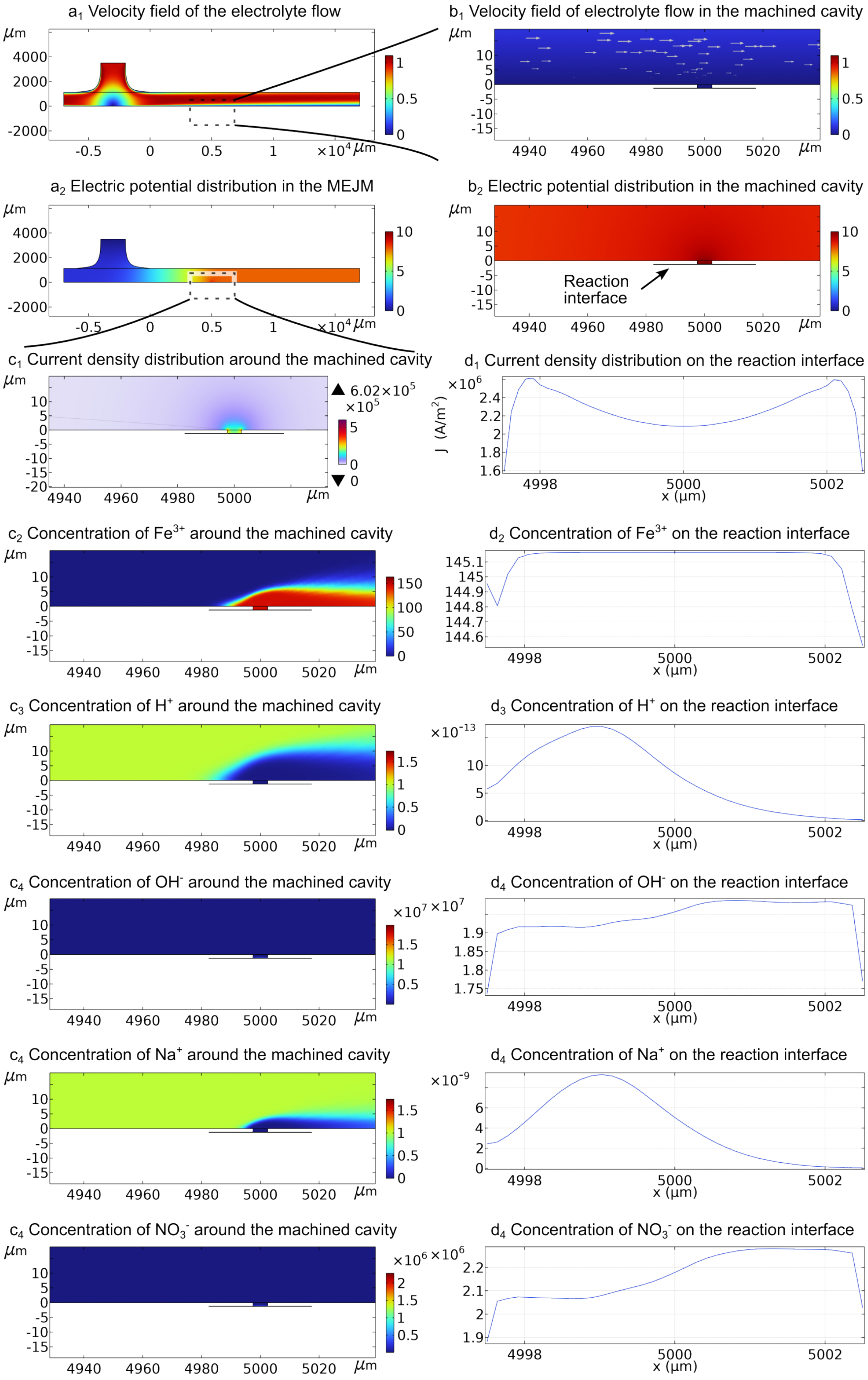
a_1 Velocity field of the electrolyte flow

b_1 Velocity field of electrolyte flow in the machined cavity

a_2 Electric potential distribution in the MEJM

b_2 Electric potential distribution in the machined cavity

c_1 Current density distribution around the machined cavity

d_1 Current density distribution on the reaction interface

c_2 Concentration of Fe^{3+} around the machined cavity

d_2 Concentration of Fe^{3+} on the reaction interface

c_3 Concentration of H^+ around the machined cavity

d_3 Concentration of H^+ on the reaction interface

c_4 Concentration of OH^- around the machined cavity

d_4 Concentration of OH^- on the reaction interface

c_4 Concentration of Na^+ around the machined cavity

d_4 Concentration of Na^+ on the reaction interface

c_4 Concentration of NO_3^- around the machined cavity

d_4 Concentration of NO_3^- on the reaction interface

Figure A1. Simulation results @ t=0 s. (a_1): velocity field of the electrolyte flow; (b_1): velocity field of electrolyte flow in the machined cavity; (a_2) electric potential distribution in the MEJM; (b_2) electric potential distribution (A/m^2) in the machined cavity; (c_1) normal current density distribution around the machined cavity; (d_1): normal current density distribution on the reaction interface; $(c_2) - (c_4)$: concentration (mol/m^3) of Fe^{3+}, H^+, OH^-, Na^+, and $NO_3{}^-$ around the machined cavity; $(d_2) - (d_4)$: concentration (mol/m^3) of Fe^{3+}, H^+, OH^-, Na^+, and $NO_3{}^-$ on the reaction interface

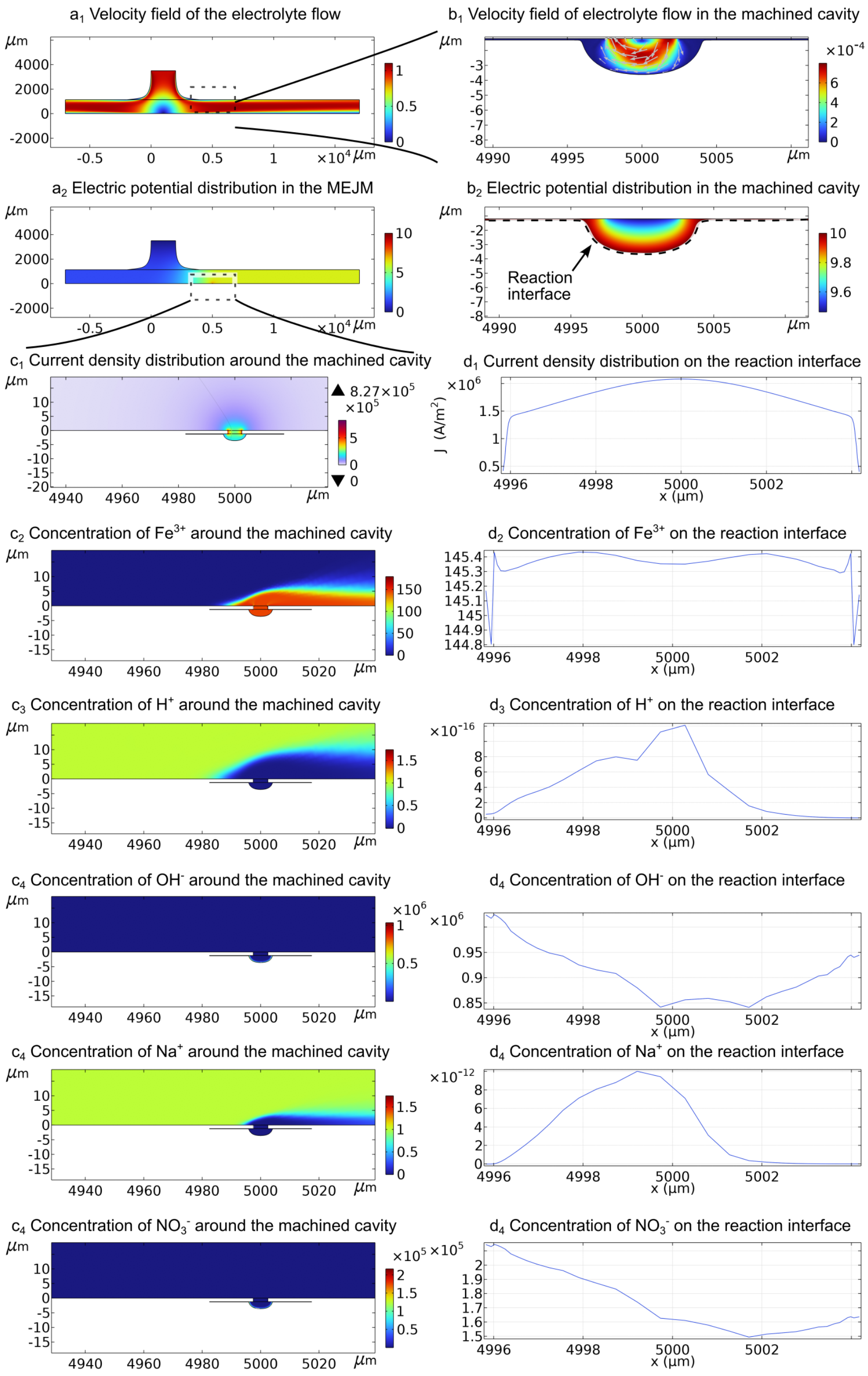

Figure A2. Simulation results @ t=1 s. (a_1): velocity field of the electrolyte flow; (b_1): velocity field of electrolyte flow in the machined cavity; (a_2) electric potential distribution in the MEJM; (b_2) electric potential distribution (A/m^2) in the machined cavity; (c_1) normal current density distribution around the machined cavity; (d_1): normal current density distribution on the reaction interface; $(c_2) - (c_4)$: concentration (mol/m^3) of Fe^{3+}, H^+, OH^-, Na^+, and $NO_3{}^-$ around the machined cavity; $(d_2) - (d_4)$: concentration (mol/m^3) of Fe^{3+}, H^+, OH^-, Na^+, and $NO_3{}^-$ on the reaction interface

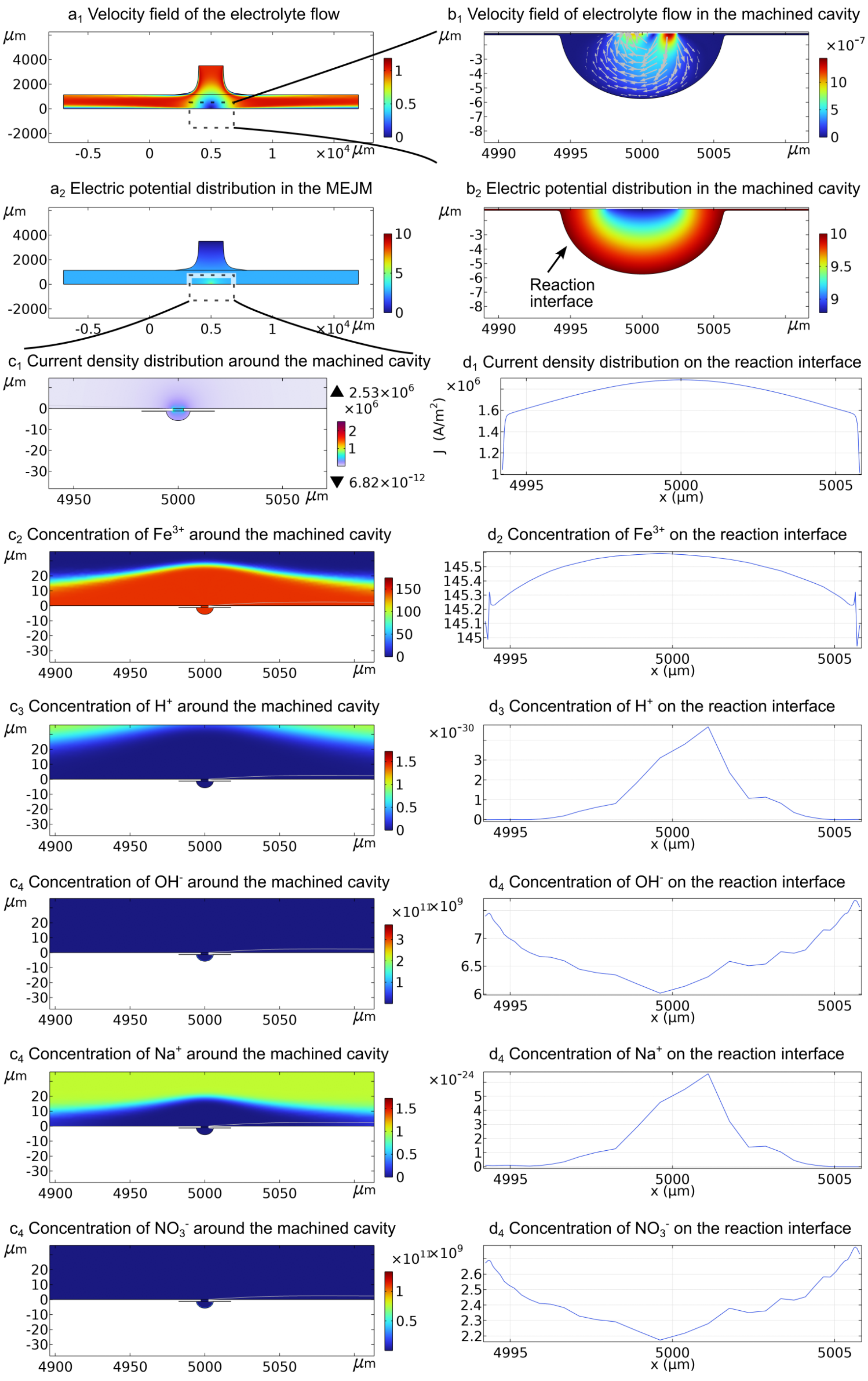

a$_1$ Velocity field of the electrolyte flow

b$_1$ Velocity field of electrolyte flow in the machined cavity

a$_2$ Electric potential distribution in the MEJM

b$_2$ Electric potential distribution in the machined cavity

c$_1$ Current density distribution around the machined cavity

d$_1$ Current density distribution on the reaction interface

c$_2$ Concentration of Fe^{3+} around the machined cavity

d$_2$ Concentration of Fe^{3+} on the reaction interface

c$_3$ Concentration of H$^+$ around the machined cavity

d$_3$ Concentration of H$^+$ on the reaction interface

c$_4$ Concentration of OH$^-$ around the machined cavity

d$_4$ Concentration of OH$^-$ on the reaction interface

c$_4$ Concentration of Na$^+$ around the machined cavity

d$_4$ Concentration of Na$^+$ on the reaction interface

c$_4$ Concentration of NO$_3^-$ around the machined cavity

d$_4$ Concentration of NO$_3^-$ on the reaction interface

Figure A3. Simulation results @ t=2 s. (a$_1$): velocity field of the electrolyte flow; (b$_1$): velocity field of electrolyte flow in the machined cavity; (a$_2$) electric potential distribution in the MEJM; (b$_2$) electric potential distribution (A/m^2) in the machined cavity; (c$_1$) normal current density distribution around the machined cavity; (d$_1$): normal current density distribution on the reaction interface; (c$_2$) − (c$_4$): concentration (mol/m^3) of Fe^{3+}, H$^+$, OH$^-$, Na$^+$, and NO$_3{}^-$ around the machined cavity; (d$_2$) − (d$_4$): concentration (mol/m^3) of Fe^{3+}, H$^+$, OH$^-$, Na$^+$, and NO$_3{}^-$ on the reaction interface

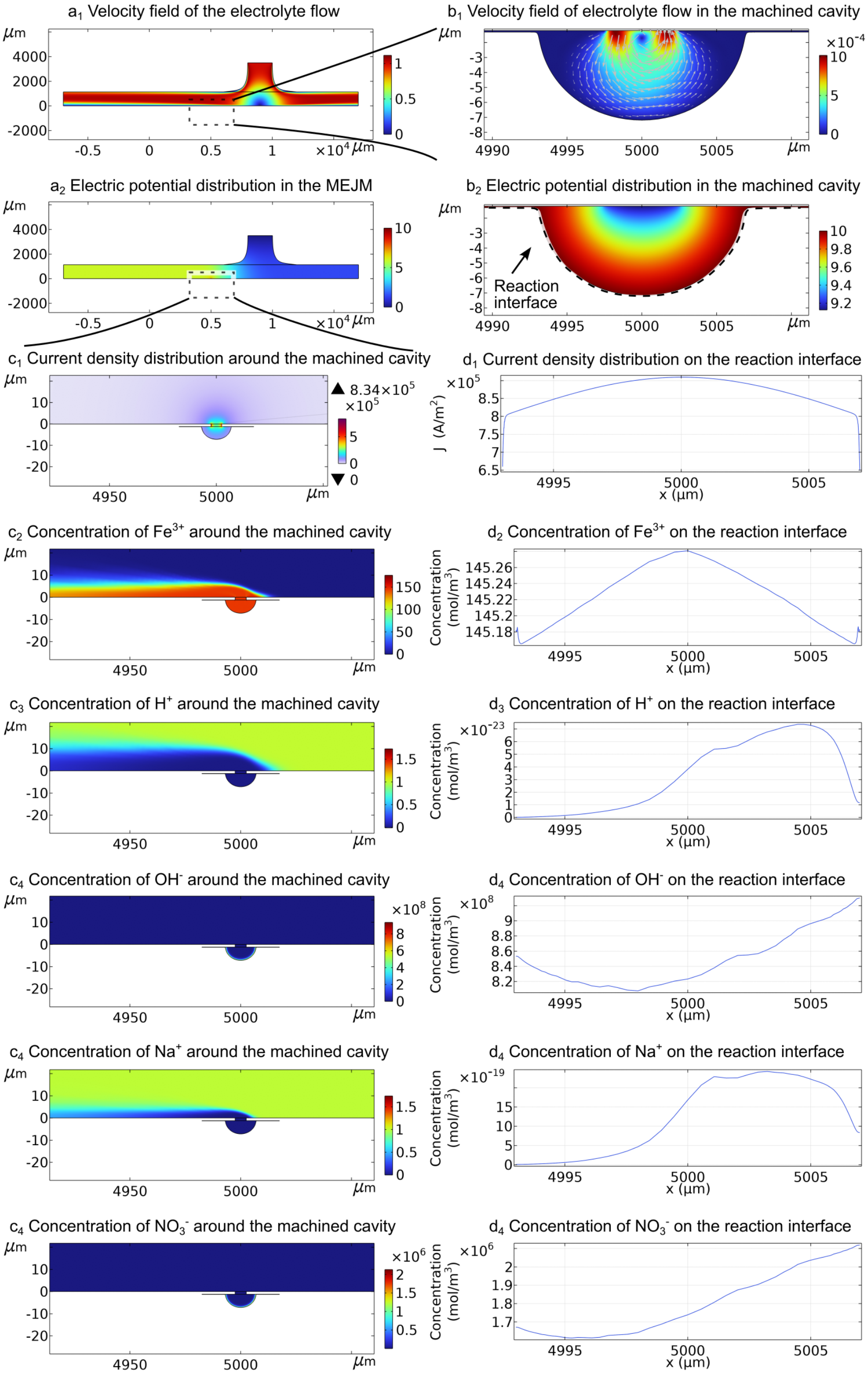

Figure A4. Simulation results @ t=3 s. (a_1): velocity field of the electrolyte flow; (b_1): velocity field of electrolyte flow in the machined cavity; (a_2) electric potential distribution in the MEJM; (b_2) electric potential distribution (A/m^2) in the machined cavity; (c_1) normal current density distribution around the machined cavity; (d_1): normal current density distribution on the reaction interface; $(c_2) - (c_4)$: concentration (mol/m^3) of Fe^{3+}, H^+, OH^-, Na^+, and $NO_3{}^-$ around the machined cavity; $(d_2) - (d_4)$: concentration (mol/m^3) of Fe^{3+}, H^+, OH^-, Na^+, and $NO_3{}^-$ on the reaction interface

References

1. Rehman, M.M.U.; Cheema, T.A.; Ahmad, F.; Abbas, A.; Malik, M.S. Numerical Investigation of Heat Transfer Enhancement and Fluid Flow Characteristics in a Microchannel Heat Sink with Different Wall/Design Configurations of Protrusions/Dimples. *Heat and Mass Transfer* **2020**, *56*, 239–255. https://doi.org/10.1007/s00231-019-02697-9.
2. Zhang, P.; Rao, Y.; Xie, Y.; Zhang, M. Turbulent Flow Structure and Heat Transfer Mechanisms over Surface Vortex Structures of Micro V-shaped Ribs and Dimples. *International Journal of Heat and Mass Transfer* **2021**, *178*, 121611. https://doi.org/10.1016/j.ijheatmasstransfer.2021.121611.
3. Heidarzadeh, A.; Mironov, S.; Kaibyshev, R.; Çam, G.; Simar, A.; Gerlich, A.; Khodabakhshi, F.; Mostafaei, A.; Field, D.P.; Robson, J.D.; et al. Friction Stir Welding/Processing of Metals and Alloys: A Comprehensive Review on Microstructural Evolution. *Progress in Materials Science* **2021**, *117*, 100752. https://doi.org/10.1016/j.pmatsci.2020.100752.
4. Bai, X.; Li, J.; Zhu, L.; Wang, L. Effect of Cu Content on Microstructure, Mechanical and Anti-Fouling Properties of TiSiN-Cu Coating Deposited by Multi-Arc Ion Plating. *Applied Surface Science* **2018**, *427*, 444–451. https://doi.org/10.1016/j.apsusc.2017.08.176.
5. Tang, M.; Zheng, L.; Hou, D.; Jia, X.; Wang, J. Microstructure Design and Construction of Anti-Wetting and Anti-Fouling Multifunctional Janus Membrane for Robust Membrane Distillation. *Chemical Engineering Journal* **2022**, *430*, 132973. https://doi.org/10.1016/j.cej.2021.132973.
6. Vignesh, G.; Barik, D.; Aravind, S.; Ragupathi, P.; Arun, M. An Experimental Study on Machining of AISI H - 13 Steel Using Dimple-Textured and Non-Textured Tungsten Carbide Cutting Tools. *IOP Conference Series: Materials Science and Engineering* **2021**, *1017*, 012021. https://doi.org/10.1088/1757-899X/1017/1/012021.
7. Patel, K.; Liu, G.; Shah, S.R.; Özel, T. Effect of Micro-Textured Tool Parameters on Forces, Stresses, Wear Rate, and Variable Friction in Titanium Alloy Machining. *Journal of Manufacturing Science and Engineering* **2019**, *142*. https://doi.org/10.1115/1.4045554.
8. Zhang, J.; Song, B.; Wei, Q.; Bourell, D.; Shi, Y. A Review of Selective Laser Melting of Aluminum Alloys: Processing, Microstructure, Property and Developing Trends. *Journal of Materials Science & Technology* **2019**, *35*, 270–284. https://doi.org/10.1016/j.jmst.2018.09.004.
9. Syahputra, H.P.; Ko, T.J. Application of Image Processing to Micro-Milling Process for Surface Texturing. *International Journal of Precision Engineering and Manufacturing* **2013**, *14*, 1507–1512. https://doi.org/10.1007/s12541-013-0203-y.
10. Li, Z.; Bai, J.; Cao, Y.; Wang, Y.; Zhu, G. Fabrication of Microelectrode with Large Aspect Ratio and Precision Machining of Micro-Hole Array by Micro-EDM. *Journal of Materials Processing Technology* **2019**, *268*, 70–79. https://doi.org/10.1016/j.jmatprotec.2019.01.009.
11. Saxena, K.K.; Qian, J.; Reynaerts, D. A Review on Process Capabilities of Electrochemical Micromachining and Its Hybrid Variants. *International Journal of Machine Tools and Manufacture* **2018**, *127*, 28–56. https://doi.org/10.1016/j.ijmachtools.2018.01.004.
12. Kunar, S.; Bhattacharyya, B. Investigation on Surface Structuring Generated by Electrochemical Micromachining. *Advances in Manufacturing* **2017**, *5*, 217–230. https://doi.org/10.1007/s40436-017-0186-5.
13. Chandrasekhar, S.; Prasad, N. Multi-Response Optimization of Electrochemical Machining Parameters in the Micro-Drilling of AA6061-TiB2in Situ Composites Using the Entropy–VIKOR Method. *Proceedings of the Institution of Mechanical Engineers, Part B: Journal of Engineering Manufacture* **2020**, *234*, 1311–1322. https://doi.org/10.1177/0954405420911539.
14. Anasane, S.S.; Bhattacharyya, B. Experimental Investigation into Fabrication of Microfeatures on Titanium by Electrochemical Micromachining. *Advances in Manufacturing* **2016**, *4*, 167–177. https://doi.org/10.1007/s40436-016-0145-6.
15. Wang, F.; Zhao, J.; Lv, Y.; Fu, X.; Kang, M.; Tian, Z. Sheet Cathode Design and Experimental Study on the Electrochemical Machining of Deep Narrow Slots in TB6 Titanium Alloy. *Proceedings of the Institution of Mechanical Engineers, Part B: Journal of Engineering Manufacture* **2020**, *234*, 801–813. https://doi.org/10.1177/0954405419883078.
16. Fan, G.; Chen, X.; Saxena, K.K.; Liu, J.; Guo, Z. Jet Electrochemical Micromachining of Micro-Grooves with Conductive-Masked Porous Cathode. *Micromachines* **2020**, *11*, 557. https://doi.org/10.3390/mi11060557.
17. Hao, X.; Wang, L.; Wang, Q.; Guo, F.; Tang, Y.; Ding, Y.; Lu, B. Surface Micro-Texturing of Metallic Cylindrical Surface with Proximity Rolling-Exposure Lithography and Electrochemical Micromachining. *Applied Surface Science* **2011**, *257*, 8906–8911. https://doi.org/10.1016/j.apsusc.2011.05.061.

18. Qu, N.; Chen, X.; Li, H.; Zeng, Y. Electrochemical Micromachining of Micro-Dimple Arrays on Cylindrical Inner Surfaces Using a Dry-Film Photoresist. *Chinese Journal of Aeronautics* **2014**, *27*, 1030–1036. https://doi.org/10.1016/j.cja.2014.03.012.
19. Qu, N.S.; Zhang, X.F.; Chen, X.L.; Li, H.S.; Zhu, D. Modified Microscale Pattern Transfer without Photolithography of Substrates. *Journal of Materials Processing Technology* **2015**, *218*, 71–79. https://doi.org/10.1016/j.jmatprotec.2014.11.040.
20. Goel, H.; Pandey, P.M. Performance Evaluation of Different Variants of Jet Electrochemical Micro-Drilling Process. *Proceedings of the Institution of Mechanical Engineers, Part B: Journal of Engineering Manufacture* **2018**, *232*, 451–464. https://doi.org/10.1177/0954405416646689.
21. Ming, W.; Zhongninga, G.; Junfeng, H.; Xiaolei, C. Modeling and Simulation of the Material Removal Process in Electrolyte Jet Machining of Mass Transfer in Convection and Electric Migration. *Procedia CIRP* **2018**, *68*, 488–492. https://doi.org/10.1016/j.procir.2017.12.079.
22. Mitchell-Smith, J.; Speidel, A.; Clare, A.T. Advancing Electrochemical Jet Methods through Manipulation of the Angle of Address. *Journal of Materials Processing Technology* **2018**, *255*, 364–372. https://doi.org/10.1016/j.jmatprotec.2017.12.026.
23. Hackert-Oschätzchen, M.; Meichsner, G.; Zinecker, M.; Martin, A.; Schubert, A. Micro Machining with Continuous Electrolytic Free Jet. *Precision Engineering* **2012**, *36*, 612–619. https://doi.org/10.1016/j.precisioneng.2012.05.003.
24. Shen, Y.; Lv, Y.; Li, B.; Huang, R.; Yu, B.; Wang, W.; Li, C.; Xu, J. Reciprocating Electrolyte Jet with Prefabricated-Mask Machining Micro-Dimple Arrays on Cast Iron Cylinder Liner. *Journal of Materials Processing Technology* **2019**, *266*, 329–338. https://doi.org/10.1016/j.jmatprotec.2018.11.009.
25. Wu, M.; Liu, J.; He, J.; Chen, X.; Guo, Z. Fabrication of Surface Microstructures by Mask Electrolyte Jet Machining. *International Journal of Machine Tools and Manufacture* **2020**, *148*, 103471. https://doi.org/10.1016/j.ijmachtools.2019.103471.
26. Wu, M.; Kumar Saxena, K.; Guo, Z.; Qian, J.; Reynaerts, D. Fast Fabrication of Complex Surficial Micro-Features Using Sequential Lithography and Jet Electrochemical Machining. *Micromachines* **2020**, *11*, 948. https://doi.org/10.3390/mi11100948.
27. Qian, S.; Zhu, D.; Qu, N.; Li, H.; Yan, D. Generating Micro-Dimples Array on the Hard Chrome-Coated Surface by Modified through Mask Electrochemical Micromachining. *The International Journal of Advanced Manufacturing Technology* **2010**, *47*, 1121–1127. https://doi.org/10.1007/s00170-009-2246-x.